7-17-2017

Ionic Liquid-Assisted Microwave Synthesis of Solid Solutions of Perovskite Sr1-xBaxSnO3 for Photocatalytic Applications

Tarek Alammar
Iowa State University, talammar@iastate.edu

Igor Slowing
Iowa State University, islowing@iastate.edu

Jim Anderegg
Ames Laboratory

Anja Mudring
Iowa State University, mudring@iastate.edu

Ionic Liquid-Assisted Microwave Synthesis of Solid Solutions of Perovskite Sr1-xBaxSnO3 for Photocatalytic Applications

Abstract

Nanocrystalline $Sr_{1-x}Ba_xSnO_3$ (x=0, 0.2, 0.4, 0.8, 1) perovskite photocatalysts were prepared by microwave synthesis in an ionic liquid (IL) and subsequent heat-treatment. The influence of the Sr/Ba substitution on the structure, crystallization, morphology, and photocatalytic efficiency was investigated and the samples were fully characterized. On the basis of X-ray diffraction results, as the Ba content in the $SrSnO_3$ lattice increases, a symmetry increase was observed from the orthorhombic perovskite structure for $SrSnO_3$ to the cubic $BaSnO_3$ structure. The analysis of the sample morphology by SEM reveals that the $Sr_{1-x}Ba_xSnO_3$ samples favor the formation of nanorods (500 nm–5 μm in diameter and several micrometers long). The photophysical properties were examined by UV/Vis diffuse reflectance spectroscopy. The band gap decreases from 3.85 to 3.19 eV with increasing Ba^{2+} content. Furthermore, the photocatalytic properties were evaluated for the hydroxylation of terephthalic acid (TA). The order of the activities for TA hydroxylation was $Sr_{0.8}Ba_{0.2}SnO_3$>$SrSnO_3$>$BaSnO_3$>$Sr_{0.6}Ba_{0.4}SnO_3$>$Sr_{0.2}Ba_{0.8}SnO_3$. The highest photocatalytic activity was observed for $Sr_{0.8}Ba_{0.2}SnO_3$, and this can be attributed to the synergistic impacts of the modification of the crystal structure and morphology, the relatively large surface area associated with the small crystallite size, and the suitable band gap and band-edge position.

Disciplines

Chemistry | Materials Science and Engineering

Comments

This article is published as Mudring, Anja Verena, Tarek Alammar, Igor Slowing, and Jim Anderegg. "Ionic Liquid-Assisted Microwave Synthesis of Solid Solutions of Perovskite Sr1-xBaxSnO3 for Photocatalytic Applications." ChemSusChem (2017). doi: 10.1002/cssc.201700615. Posted with permission.

ChemPubSoc Europe

DOI: 10.1002/cssc.201700615

CHEMSUSCHEM Full Papers

Ionic-Liquid-Assisted Microwave Synthesis of Solid Solutions of $Sr_{1-x}Ba_xSnO_3$ Perovskite for Photocatalytic Applications

Tarek Alammar,[a, b] Igor I. Slowing,[b] Jim Anderegg,[b] and Anja-Verena Mudring*[a, b, c]

Nanocrystalline $Sr_{1-x}Ba_xSnO_3$ ($x = 0$, 0.2, 0.4, 0.8, 1) perovskite photocatalysts were prepared by microwave synthesis in an ionic liquid (IL) and subsequent heat-treatment. The influence of the Sr/Ba substitution on the structure, crystallization, morphology, and photocatalytic efficiency was investigated and the samples were fully characterized. On the basis of X-ray diffraction results, as the Ba content in the $SrSnO_3$ lattice increases, a symmetry increase was observed from the orthorhombic perovskite structure for $SrSnO_3$ to the cubic $BaSnO_3$ structure. The analysis of the sample morphology by SEM reveals that the $Sr_{1-x}Ba_xSnO_3$ samples favor the formation of nanorods (500 nm–5 μm in diameter and several micrometers long). The photophysical properties were examined by UV/Vis diffuse reflectance spectroscopy. The band gap decreases from 3.85 to 3.19 eV with increasing Ba^{2+} content. Furthermore, the photocatalytic properties were evaluated for the hydroxylation of terephthalic acid (TA). The order of the activities for TA hydroxylation was $Sr_{0.8}Ba_{0.2}SnO_3 > SrSnO_3 > BaSnO_3 > Sr_{0.6}Ba_{0.4}SnO_3 > Sr_{0.2}Ba_{0.8}SnO_3$. The highest photocatalytic activity was observed for $Sr_{0.8}Ba_{0.2}SnO_3$, and this can be attributed to the synergistic impacts of the modification of the crystal structure and morphology, the relatively large surface area associated with the small crystallite size, and the suitable band gap and band-edge position.

Introduction

Perovskite alkaline-earth stannates $ASnO_3$ (A = Sr, Ba) and their corresponding solid solutions have attracted increasing research interest in recent years owing to their unique physical and chemical properties and their importance as functional materials in a wide range of scientific and technological applications. These applications range from photocatalysis, light-emitting devices, relaxor ferroelectrics, and fuel cells to dielectric materials in capacitors, Li-ion batteries, chemical sensors, and thermally stable capacitors.[1,2]

Conventionally, these materials are prepared through solid-state reactions by sintering mechanical mixtures of their component binary oxides or the corresponding carbonates and SnO_2 at high temperatures (> 1000 °C) for prolonged times.[3] Despite the simplicity of this method, it requires high temperature and yields products with low homogeneity, uncontrollable morphology, large grains, and low surface areas, and undesired secondary phases such as carbonates are often produced.[4] Recently, different methods have been used to overcome the mentioned drawbacks of theses solid-state reactions. Yuan et al.[5] reported the preparation of $Ba_{1-x}Sr_xSnO_3$ ($x = 0$, 0.25, 0.5, 0.75, 1) by a polymerized complex method in ethylene glycol at 1000 °C. Stanulis et al. produced $ASnO_3$ (Ca, Sr, Ba) by aqueous sol–gel techniques in the presence of peroxide and nitrate oxidizing agents at 800 or 1000 °C.[6] Ahmed et al. reported the production of $ASnO_3$ (Sr, Ba) by microemulsion methods through two procedures with 1-hexadecyltrimethylammonium bromide as the surfactant, 1-butanol as the cosurfactant, and 2,2,4-trimethylpentane as the oil phase at 650 °C.[7] Moshtaghi et al. prepared $SrSnO_3$ through coprecipitation with bis(salicylaldehydato)strontium as the precursor at 900 °C.[8] Wang et al. reported the preparation of $SrSnO_3$ by a combustion method at 1000 °C,[9] and Chen et al. synthesized $SrSnO_3$ by calcination of the hydrothermally prepared $SrSn(OH)_6$ at 1100 °C.[10]

However, all of these methods require elevated temperatures, relatively long reaction times, additional capping agents, and sometimes expensive and quite toxic raw materials including volatile compounds as starting materials. Therefore, the development of a mild, efficient method to produce alkaline-earth stannate perovskite photocatalysts without the need for additional surfactants or templates and harsh reaction conditions is highly desirable.

[a] Dr. T. Alammar, Prof. Dr. A.-V. Mudring
Department of Materials Science and Engineering, Iowa State University
Ames, IA 50011 (USA)

[b] Dr. T. Alammar, Dr. I. I. Slowing, J. Anderegg, Prof. Dr. A.-V. Mudring
The Ames Laboratory, U.S. Department of Energy
Ames, IA 50011 (USA)

[c] Prof. Dr. A.-V. Mudring
Department of Materials and Environmental Chemistry
Stockholm University
Svante Arrhenius väg 16C, 106 91 Stockholm (Sweden)
E-mail: anja-verena.mudring@mmk.su.se

Supporting Information and the ORCID identification number(s) for the author(s) of this article can be found under https://doi.org/10.1002/cssc.201700615.

The ionic-liquid-assisted microwave method has special advantages for materials preparation and is emerging as an alternative to conventional methods. The use of this method has increased significantly in recent years because of its strengths such as shorter reaction times, high reaction rates, energy saving, uniform heating, and good product yields.[11] The microwave heating process is based on the conversion of electromagnetic energy to thermal energy through dipolar polarization and ion-conduction mechanisms. The reaction medium must show a dipole moment to create heat under microwave irradiation.[12] Room-temperature ionic liquids (RTILs) are molten salts with melting points of less than 100 °C and consist of asymmetric organic cations and inorganic or organic anions. Thus, ion conduction and dipolar polarization both contribute to the heating process if an ionic liquid is used at the reaction medium. Ionic liquids (ILs) have been promoted as green solvents as their vapor pressures are often low.[13] Moreover, in inorganic nanomaterials synthesis, ILs have the benefit that they can act as electronic as well as a steric particle stabilizers and thereby suppress particle growth.[14,15] The unprecedented potential of ILs for the efficient absorption of microwave radiation makes them particularly attractive media for microwave reactions. This superior behavior of ILs as heating media under microwave irradiation can be attributed to their unique structural compositions, which consist of large ions with high polarizability and conductivity, and this leads to faster, more uniform, and more effective heat-transfer processes.[16] The advantages of combining ILs with microwave heating go beyond the mere heating process and particle stabilization. Through the templating effect of the IL, it is possible to tune and control the particle size, morphology, and, for polymorphic materials, the crystal phase.[17] With respect to the microwave synthesis of alkali-metal stannates, Bohnemann et al. reported the preparation of $SrSnO_3$ through the microwave-assisted calcination of $SrSn(OH)_6$ in water at temperatures in the range 500–1100 °C. However, $SrCO_3$ was observed as a secondary phase.[18] Wang et al. prepared $MSnO_3$ (Ca, Sr, Ba) by a microwave hydrothermal method and subsequent heat treatment at 800 °C.[19]

Despite the promise of the coupling of microwave synthesis with ILs in the field of nanosynthesis, to our knowledge, there are no studies available on the use of ionic-liquid-assisted microwave methods for the synthesis of $SrSnO_3$, $BaSnO_3$, or their solid solutions $Sr_{1-x}Ba_xSnO_3$. Thus, herein we report an effective and versatile route for the preparation of $Sr_{1-x}Ba_xSnO_3$ ($x=0$, 0.2, 0.4, 0.8, 1) perovskite photocatalysts by such a microwave-assisted ionic-liquid method. The ILs acts as the solvent, heat-transfer medium, template, and particle stabilizer. The impact of the substitution of Ba for Sr in $SrSnO_3$ on the shape, crystallinity, energy band structure, and catalytic activity for the photohydroxylation of terephthalic acid was studied in detail.

Results and Discussion

The powder XRD patterns of the $Sr_{1-x}Ba_xSnO_3$ samples (Figure 1) show that all of the diffraction peaks can be indexed to $SrSnO_3$ in the orthorhombic space group *Pnma* (PDF 77–1798) with lattice constants $a=5.715(6)$ Å, $b=8.077(6)$ Å, and $c=5.717(6)$ Å or $BaSnO_3$ in the cubic space group $Pm\bar{3}m$ (PDF 15-780) with a lattice constant of $a=4.117(7)$ Å. No impurity peaks of the binary oxides SnO_2, BaO, and SrO or carbonate or pyrochlore phases were detected. Moreover, all of the diffraction peaks are shifted towards lower diffraction angles (2θ) as the Ba concentration increases from $x=0$ to 1 (Figure 1, bottom).

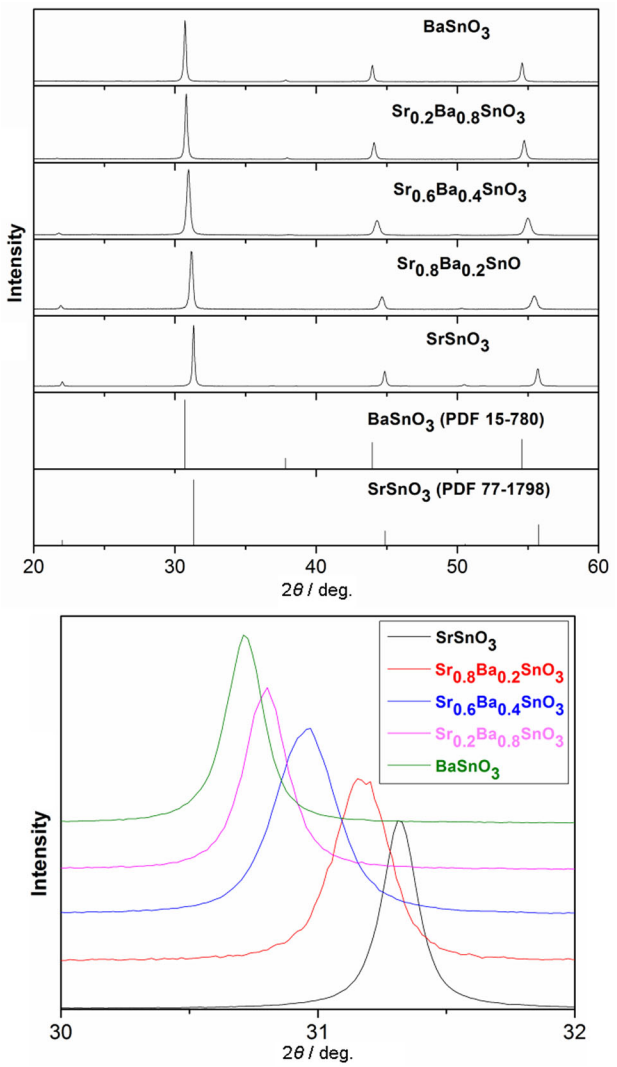

Figure 1. Top: XRD patterns of $Sr_{1-x}Ba_xSnO_3$ samples compared with those of $SrSnO_3$ (PDF 77-1798) and $BaSnO_3$ (PDF 15-780). Bottom: enlarged view of the $2\theta=30$–$32°$ region.

This linear shift obeys the Vegard rule and indicates that the samples are solid solutions of $SrSnO_3$ and $BaSnO_3$ with homogeneous cation distributions and not physical mixtures of $SrSnO_3$ and $BaSnO_3$. The trend can be attributed to the different sizes of the Sr^{2+} and Ba^{2+} cations, as the radius of the Sr^{2+} ion of 144 pm is smaller than that of the Ba^{2+} ion of 161 pm.[20] The increased substitution of Sr^{2+} cations by Ba^{2+} cations is associated with the change of the space-group symmetry from *Pnma* ($x=0$, 0.2) to *Imma* ($x=0.4$) and finally to $Pm\bar{3}m$ ($x=0.8$, 1). The increase in symmetry is driven by the decrease in

the tilting of the Sn^{4+}-centered octahedra as a result of the improved match between the dodecahedral cavities in the corner-sharing octahedral network and the alkaline-earth cations. The cell parameters, cell volume, and space group of the solid-solution samples were obtained from Rietveld refinement with the FULLPROF program by incorporating a pseudo-Voigt peak-shape function (Table 1). The cell parameters increase with increasing Ba^{2+} doping content and, likewise, the unit-cell volume increases (Figure SI-1). The average crystallite sizes were estimated with the Debye–Scherrer formula from the full width at half-maximum (FWHM) values of the most intense diffraction peaks (Table 2). The crystal sizes of the samples ranges from 32.65 nm for $Sr_{0.6}Ba_{0.4}SnO_3$ to 54.06 nm for $SrSnO_3$.

Table 1. Pseudocubic subcell parameters and cell volume of $Sr_{1-x}Ba_xSnO_3$ samples. $a = a_0/\sqrt{2}$, $b = b_0/2$, $C = C_0/\sqrt{2}$ for orthorhombic *Pnma* and *Imma*.

Sample	*a* [Å]	*b* [Å]	*c* [Å]	Volume [Å^3]	Space group
$SrSnO_3$	4.0415(4)	4.0388(3)	4.0425(4)	65.98 ± 0.045	*Pnma*
$Sr_{0.8}Ba_{0.2}SnO_3$	4.0635(3)	4.0532(1)	4.0581(2)	66.84 ± 0.088	*Pnma*
$Sr_{0.6}Ba_{0.4}SnO_3$	4.08616(1)	4.0984(3)	4.0879(1)	68.46 ± 0.002	*Imma*
$Sr_{0.2}Ba_{0.8}SnO_3$	4.1070(1)	4.1070(1)	4.1070(1)	69.27 ± 0.003	$Pm\bar{3}m$
$BaSnO_3$	4.1176(7)	4.1176(7)	4.1176(7)	69.81 ± 0.002	$Pm\bar{3}m$

Table 2. Estimated crystallite size from the Scherrer equation and crystallite strain from the W–H equation.

Sample	Crystallite size [nm]	Crystallite strain (ε_{str})
$SrSnO_3$	54.06 ± 1	0.0018
$Sr_{0.8}Ba_{0.2}SnO_3$	35.38 ± 1	0.0034
$Sr_{0.6}Ba_{0.4}SnO_3$	32.65 ± 1	0.0032
$Sr_{0.2}Ba_{0.8}SnO_3$	47.27 ± 1	0.0014
$BaSnO_3$	53.25 ± 1	0.0007

The crystallite strain values of the $Sr_{1-x}Ba_xSnO_3$ samples were estimated with the Williamson–Hall (W–H) equation.[21] A plot of $B_{hkl}\cos\theta$ against $4\sin\theta$ for the $Sr_{1-x}Ba_xSnO_3$ samples is shown in Figure 2. The strain ε can be derived from such a graph as the slope of the linear fit (Table 2). The crystallite strain values range from 0.0007 for $BaSnO_3$ to 0.0034 for $Sr_{0.8}Ba_{0.2}SnO_3$. The particle strain is caused by lattice distortions, which can be caused by the presence of one or more lattice-defect types such as point defects, distorted grain boundaries, dislocation concentration gradients, and stacking faults. Such lattice defects function as trapping and recombination centers for photoexcited electrons and, therefore, reduce the efficiency of the photocatalyst. The small strain values suggest the presence of few lattice defects and high crystallinity and render the materials promising for photocatalysis. On the basis of the crystallite strain values, it is evident that $BaSnO_3$ demonstrates the highest crystallinity, whereas $Sr_{0.8}Ba_{0.2}SnO_3$ is the least crystalline material.

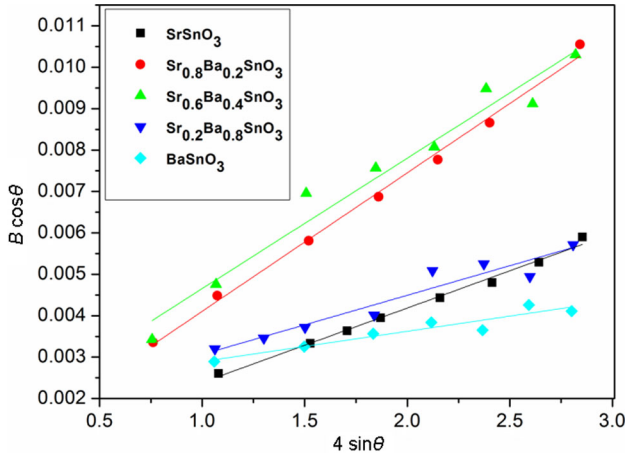

Figure 2. Williamson–Hall plots for the prepared $Sr_{1-x}Ba_xSnO_3$ samples.

The thermogravimetric analysis (TGA) curve of the as-prepared $SrSn(OH)_6$ in the temperature range from room temperature to 1050 °C is given in Figure SI-3 (see the Supporting Information). The major, rapid weight loss (exp. ≈20%; calculated 22%) can be ascribed to the dehydroxylation process of $SrSn(OH)_6$ and the formation of $SrSnO_3$. Furthermore, no further significant weight losses can be seen in the TGA curve up to 700 °C; therefore, the TGA data confirm the XRD data and demonstrate the complete conversion of the $SrSn(OH)_6$ precursor into $SrSnO_3$.[22] Similar thermal behavior was observed for the other $Sr_{1-x}Ba_xSn(OH)_6$ samples.

Representative SEM images of the $Sr_{1-x}Ba_xSnO_3$ samples are shown in Figure 3. All of the micrographs show particles with rod-shaped morphologies, diameters in the range 500 nm–5 μm, and lengths of several micrometers. As the Ba content in the lattice of $SrSnO_3$ increases, the rod diameter increases, and the rods become less homogeneous. Furthermore, the particle-

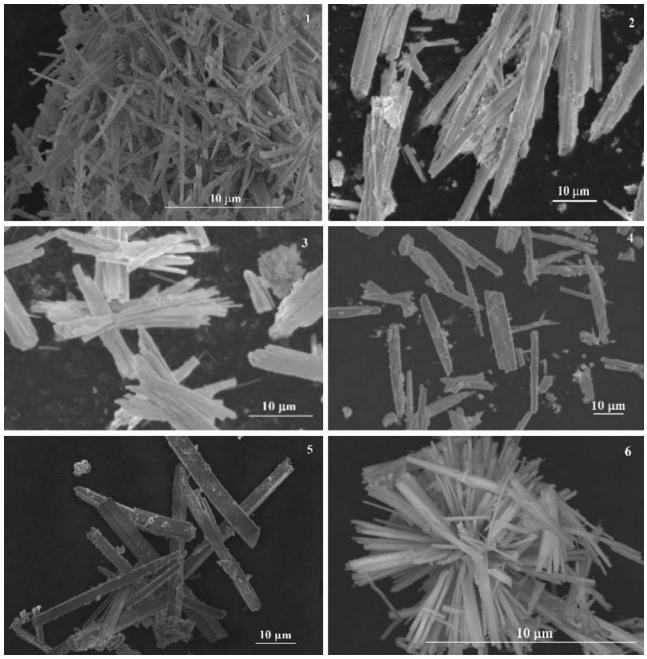

Figure 3. SEM images: (1) $SrSnO_3$, (2) $Sr_{0.8}Ba_{0.2}SnO_3$, (3) $Sr_{0.6}Ba_{0.4}SnO_3$, (4) $Sr_{0.2}Ba_{0.8}SnO_3$, (5) $BaSnO_3$, and (6) $SrSnO_3$ prepared in demineralized water without ionic liquid. Scale bars correspond to 10 μm.

size distribution becomes more polydisperse, and the shapes become more defective. The results show that Ba substitution enhances the grain growth, and the diameters evolve from a few hundred nanometers for $SrSnO_3$ to a few microns for $BaSnO_3$. The growth units of $MSn(OH)_6$ are composed of M^{2+} cations and $Sn(OH)_6^{2-}$ anions, whereas the ionic liquid 1-butyl-3-methylimidazolium bis(trifluoromethanesulfonyl)amide ($[C_4mim][Tf_2N]$) is a fluid salt consisting of a short alkylmethylimidazolium-based cation and a weakly coordinating Tf_2N^- anion. The $[C_4mim]^+$ cation has an aromatic core and can be held accountable for the electrostatic attractions with polar moieties on the surfaces of the particles. Moreover, the aromatic ring bears an acidic proton (C2–H) because of the polarization of the C=N bond and the highly polarized C2–H bond. The acidic proton can act as a bridging species through hydrogen bonding (Figure SI-4).[23]

Owing to the hydrogen-bonding interactions and π–π stacking arrangements between the imidazolium rings, the imidazolium-based ionic liquid forms 3D ionic networks with high directional polarizability through anionic and cationic supramolecular aggregates of general formula $[(C_4mim)_x(Tf_2N)_{x-n}]^{n+}[(C_4mim)_{x-n}(Tf_2N)_x]^{n-}$. The volume of the 3D regions within the ionic liquid (template effect) in addition to the electrostatic and steric repulsions tailor the sizes and shapes of the nanomaterials prepared in ILs.[24] Wang et al. used FTIR spectroscopy to demonstrate the formation of hydrogen bonds between the oxygen atoms of O–Zn moieties in ZnO nuclei and the ionic liquid $[C_2mim][BF_4]$ (C_2mim = 1-ethyl-3-methylimidazolium), as well as its important role in the occurrence of 1D ZnO growth.[25] In the presence of ZnO nanorods, the adsorption band for the C2–H moiety in the imidazolium cation was broadened and weakened compared with that for pure $[C_2mim][BF_4]$. Furthermore, if the C2–H proton in the imidazolium cation was replaced by a CH_3 group, ZnO nanoparticles (NPs) were obtained, and this finding was attributed to weaker hydrogen bonding.[25] Gutel et al. reported the preparation of ruthenium nanoparticles in 3D alkylimidazolium ionic liquids.[26] Their results suggest that the length of the side alkyl chain and the presence of the C2–H hydrogen atom of the imidazolium cation influence significantly the scale of organization and the size of the nonpolar regions in imidazolium-based ILs and, thereby, the size and size distribution of the obtained Ru NPs. If $[C_4mim][Tf_2N]$ was replaced by $[C_8mim][Tf_2N]$ (C_8mim = 1-methyl-3-octylimidazolium), the mean size of Ru NPs increased from 2.3 to 3.6 nm, as determined through TEM measurements.[26] Therefore, it can be assumed that the electrostatic and coordinative interactions of the imidazolium cations of the IL with the growth units affect the structure and surface properties and govern the growth of the $MSnO_3$ nanocrystals.

To check the influence of the ionic liquid on the morphology and phase of $SrSnO_3$, we prepared $SrSnO_3$ in demineralized water without an ionic liquid and kept the other reaction conditions unchanged. The SEM image (Figure 3, image 6) shows that the sample mostly consists of agglomerated rod-shaped particles. As no template or surfactant was used, the reduction of surface energy was the predominant factor controlling the growth and shape of the particles for this nonequilibrium kinetic growth. Apparently, the rodlike particles have a tendency to self-assemble and grow radially from the center to form brush-like particle agglomerations. The associated XRD pattern and Rietveld refinement for this pattern (Figure SI-5) show that the sample crystallizes in the orthorhombic space group *Pnma*. This experiment demonstrates the importance of the ionic liquid to the prevention of particle agglomeration and the control of the particle morphology.

The IR spectra of all of the $Sr_{1-x}Ba_xSnO_3$ samples are shown in Figure 4. All of the samples show similar spectra with a high-intensity infrared absorption band in the range between $\tilde{\nu}$ = 550 and 750 cm^{-1}, which corresponds to the vibrations of the Sn–O bonds in the stannate group $\{SnO_6\}$.[3] As shown in Figure 4 (left), this band is shifted to lower wavenumbers from 641 cm^{-1} for $SrSnO_3$ (x = 0) to 609 cm^{-1} for $BaSnO_3$ (x = 1) as the Ba^{2+} content increases, as expected owing to the increased

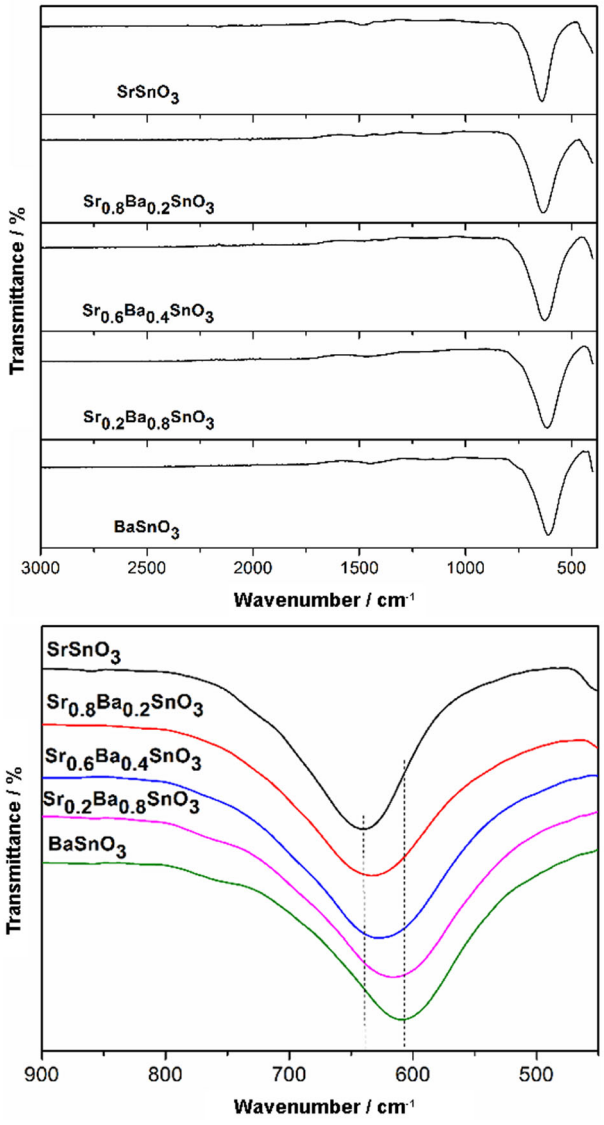

Figure 4. Top: IR spectra of the prepared $Sr_{1-x}Ba_xSnO_3$ samples. Bottom: enlarged view of the $\tilde{\nu}$ = 500–900 cm^{-1} region.

Sn–O interatomic distance and the decreased Sn–O force constant upon substitution. Importantly, no bands from carbonates (the most characteristic bands are found at $\tilde{\nu}=870$ and 1430 cm^{-1})[27] or other impurities can be observed. The identical IR spectra (Figure SI-6) of the pristine and recovered $[C_4mim][Tf_2N]$ confirm the structural stability of the ionic liquid in the reaction, specifically under microwave irradiation, and its recyclability.

The Raman spectra of the $Sr_{1-x}Ba_xSnO_3$ samples are shown in Figure 5. For $SrSnO_3$ crystallizing as an orthorhombic perov-

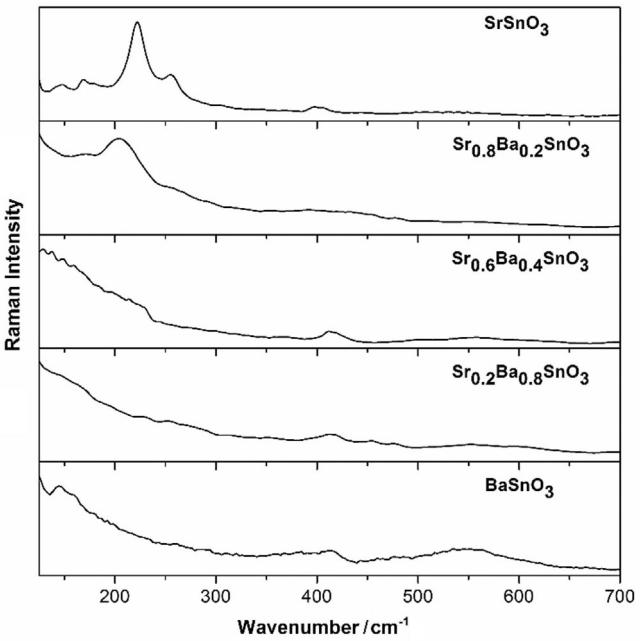

Figure 5. Raman spectra of the $Sr_{1-x}Ba_xSnO_3$ samples.

skite in the space group *Pnma*, 24 Raman-active modes at $q=0$ with $\Gamma_{Raman}=7A_g+5B_{1g}+7B_{2g}+5B_{3g}$ can be expected on the basis of factor-group analysis.[28] The active modes can be classified as two symmetric and four antisymmetric octahedral stretching modes, four bending modes, and six rotational or tilt modes of the octahedral $\{SnO_6\}$ units. The other eight modes are related to the strontium cations. Nevertheless, owing to the overlap and very low polarizabilities of some of these modes, not all of them can be observed. The bands at $\tilde{\nu}=144$ and 168 cm^{-1} are attributed to the $SrSnO_3$ network modes.

The most intense band, at $\tilde{\nu}=222$ cm^{-1}, results from the A_g mode, which corresponds to the scissoring movement of the Sn–O–Sn groups along the *c* axis. The band at $\tilde{\nu}=250$ cm^{-1} is due to the O–Sn–O bending motion within the *ab* plane and Sn–O–Sn scissoring perpendicular to the *c* axis. The low-intensity band at $\tilde{\nu}=398$ cm^{-1} is assigned to the torsional mode.[29] For $BaSnO_3$ crystallizing as a cubic perovskite with the space group $Pm\bar{3}m$, no first-order Raman-active modes are expected because of the centrosymmetric structure. Thus, the weak bands centered at $\tilde{\nu}=144$, 398, and 554 cm^{-1} can be attributed to the presence of defects in the materials such as strain, grain boundaries, oxygen vacancies, and impurity atoms, which are able to break the inversion symmetry and activate the Raman-forbidden modes.[30] For the $Sr_{1-x}Ba_xSnO_3$ ($x=0.2$–0.8) solid solutions, changes in the spectra become visible. For $x=0.2$, the same bands as those in the spectrum of $SrSnO_3$ are observed, albeit with significantly lower intensities. As *x* increases ($x=0.4$ and 0.8), the bands at $\tilde{\nu}=144$, 168, 222, and 250 cm^{-1} disappear, and the band at $\tilde{\nu}=398$ cm^{-1} becomes more intense. Additionally, the band at $\tilde{\nu}=554$ cm^{-1}, which can be attributed to the Sn–O stretching mode and is not present for $SrSnO_3$ and $Sr_{0.8}Ba_{0.2}SnO_3$, increases in intensity. This observation indicates the gradual increase of the A–O bond length as the Ba^{2+} concentration increases, in parallel with Sn–O bond elongation.

X-ray photoelectron spectroscopy (XPS) was used to check the elemental composition and the oxidation state of each element in the $Sr_{1-x}Ba_xSnO_3$ solid solutions. The XPS survey spectra of the $Sr_{1-x}Ba_xSnO_3$ solid solutions are presented in Figure 6

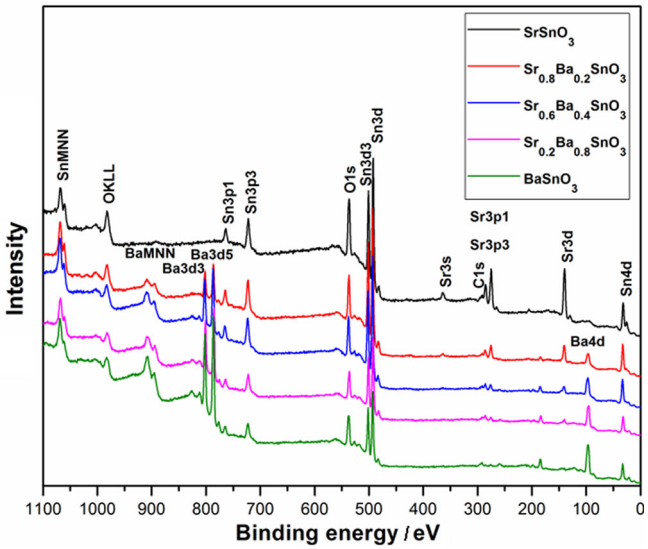

Figure 6. XPS survey scans of the $Sr_{1-x}Ba_xSnO_3$ samples.

and show the Sr, Ba, Sn, and O surface components. The binding energies (BEs) in the XPS spectra were calibrated against the C 1s signal (BE = 284.8 eV) of adventitious physisorbed carbon. The Sr 3d, Ba 3d, Sn 3d, and O 1s scans of $SrSnO_3$, $Sr_{0.8}Ba_{0.2}SnO_3$, $Sr_{0.6}Ba_{0.4}SnO_3$, $Sr_{0.2}Ba_{0.8}SnO_3$, and $BaSnO_3$ are shown in Figures 7, 8, 9, 10, and 11, respectively. The best fits of the Sr 3d XPS spectra for $Sr_{1-x}Ba_xSnO_3$ reveal that the obtained curves are mixtures of two overlapping peaks. These are assigned to $Sr\,3d_{5/2}$ at BE = 132.8–133 eV and $Sr\,3d_{3/2}$ at BE = 134.5–134.7 eV with a peak separation of 1.7 eV.

The XPS spectra for the Ba 3d contributions show two peaks at BE = 779.1–779.6 and 794.4–794.8 eV for $3d_{5/2}$ and $3d_{3/2}$, respectively. These values are in good agreement with those reported previously.[31] It is clear from Table 3 that the two Ba 3d peaks shift to lower binding energies as the Ba concentration in the $SrSnO_3$ lattice increases. The Sn 3d XPS spectra for the $Sr_{1-x}Ba_xSnO_3$ samples show two peaks at BE = 485.5–486.2 and

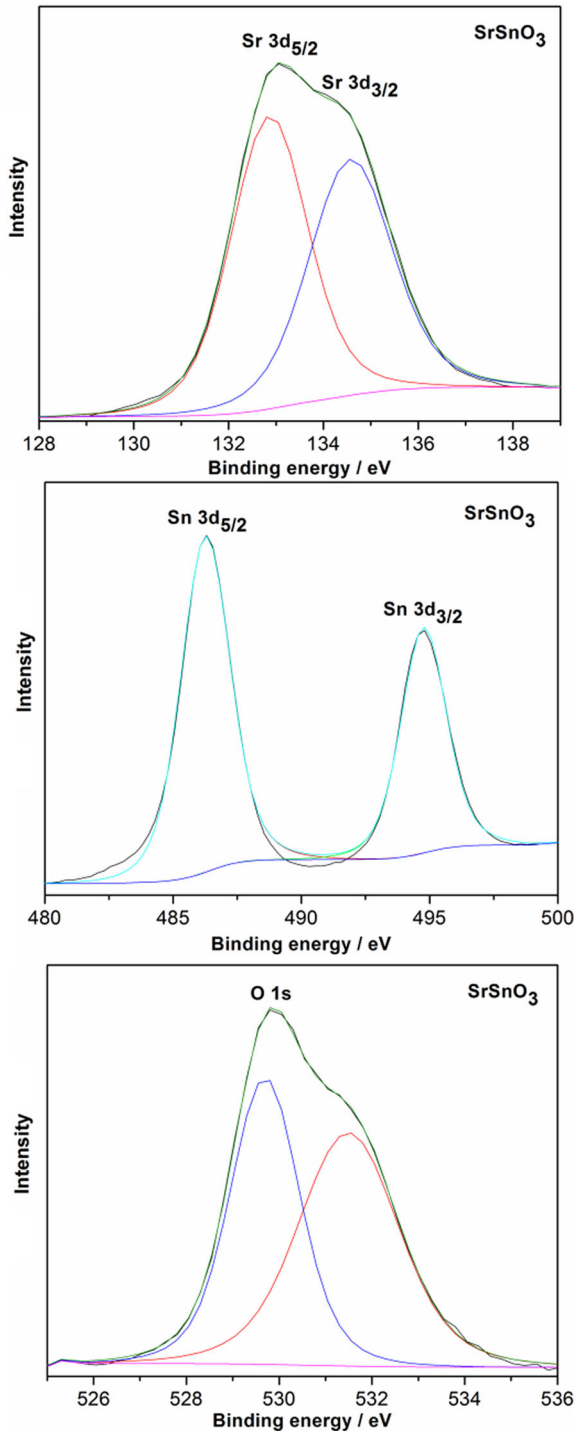

Figure 7. Detailed XPS scans of the Sr 3d, Sn 3d, and O 1s regions for $SrSnO_3$.

Table 3. XPS binding energies (±0.1) [eV] of Sn, O, Sr, and Ba in the $Sr_{1-x}Ba_xSnO_3$ samples.

Element	$SrSnO_3$	$Sr_{0.8}Ba_{0.2}SnO_3$	$Sr_{0.6}Ba_{0.4}SnO_3$	$Sr_{0.2}BaS_{0.8}nO_3$	$BaSnO_3$
Sn ($3d_{5/2}$, $3d_{3/2}$)	486.2, 494.7	486, 494.5	486, 494.5	485.9, 494.5	485.5, 494,1
O (1s)	529.7, 531,5	529.5, 531	529.5, 530.9	529.3, 530.9	529.1, 530.9
Sr ($3d_{5/2}$, $3d_{3/2}$)	132.8, 134.5	132.8, 134.3	132.8, 134.3	133, 134.7	–
Ba ($3d_{5/2}$, $3d_{3/2}$)	–	779.6, 794.8	779.5, 794.8	779.2, 794.5	779.1, 794.4

494.1–494.7 eV with a peak separation of 8.5 eV. The peaks can be attributed to Sn $3d_{5/2}$ and Sn $3d_{3/2}$, respectively. The Sn 3d peak separation in this study (8.5 eV) matches that reported for SnO_2. In addition, the presence of Sn^{II} can be ruled out because of the absence of any subpeaks among the symmetric Sn $3d_{5/2}$ and Sn $3d_{3/2}$ peaks.[32] Thus, the Sn atoms on the sample surfaces have an oxidation state of +IV. The Sn binding energy is also influenced by the incorporation of Ba^{2+} ions into the $SrSnO_3$ lattice, as can be determined from Table 3. The Sn $3d_{5/2}$ and Sn $3d_{3/2}$ BEs of $SrSnO_3$ with distorted $\{SnO_6\}$ octahedra are higher than those for $BaSnO_3$ with perfect $\{SnO_6\}$ octahedra. The distortion of the $\{SnO_6\}$ octahedra is caused by the different sizes of the Sr^{2+} and Ba^{2+} cations, which is also reflected in the changes in the BEs. The O 1s XPS spectra shows broad and asymmetric bands that can be fitted to two peaks at BE = 529.1–529.7 and 530.9–531.5 eV. The peak at BE = 529.1–529.7 eV can be attributed to the lattice O^{2-} ions. The slight decrease of the BE of the lattice O^{2-} ions with increasing Ba content can be attributed to the different electronegativities of the alkaline-earth metals.[31] The less-intense peak at BE = 531.2–531.5 eV is due to the OH^- ions adsorbed on the surface. The BEs reported in this study are in quite close agreement with those reported previously for $SrSnO_3$ and $BaSnO_3$.[33] No clear impurity peaks such as those for elements from the ionic liquids can be seen, and this confirms the purity of the samples.

The optical absorption properties of the $Sr_{1-x}Ba_xSnO_3$ samples were measured by UV/Vis diffuse reflectance spectroscopy (DRS). The DRS spectra of the $Sr_{1-x}Ba_xSnO_3$ samples are shown in Figure 12 (top). The UV/Vis spectra of the $Sr_{1-x}Ba_xSnO_3$ samples show that the absorption edges vary from $\lambda = 358$ nm for $SrSnO_3$ ($x = 0$) to $\lambda = 430$ nm for $BaSnO_3$ ($x = 1$), and this variation can be attributed to the transitions of the O 2p electrons of the valence band into Sn 5s states of the conduction band under UV light irradiation.[9] The absorption edges are estimated from the linear extrapolation of the steep part of the UV absorption toward the baseline. It can be seen from Figure 12 (top) that the absorption edge is redshifted with increasing Ba content in the $SrSnO_3$ lattice.

The optical band gaps (E_g) of the samples can be calculated from the optical absorption spectra with a Tauc plot [Eq. (1)]:

$$(\alpha h\nu)^n = B(h\nu - E_g) \quad (1)$$

where $h\nu$ is the photon energy, α is the absorption coefficient, B is related to the effective masses associated with the valence and conduction bands, and $n = 2$ for an indirect allowed transition or $n = 1/2$ for a direct allowed transition. A plot of $(\alpha h\nu)^2$ versus $h\nu$ from the spectral response gives the corresponding extrapolated E_g values. As shown in Figure 12 (bottom) and Table 4, the band gaps of the $Sr_{1-x}Ba_xSnO_3$ samples range from 3.1 eV for $BaSnO_3$ to 3.85 eV for $SrSnO_3$. This deviation in the band gaps of the samples suggests that they have different UV/Vis absorption properties that could lead to different photocatalytic properties. The gradual

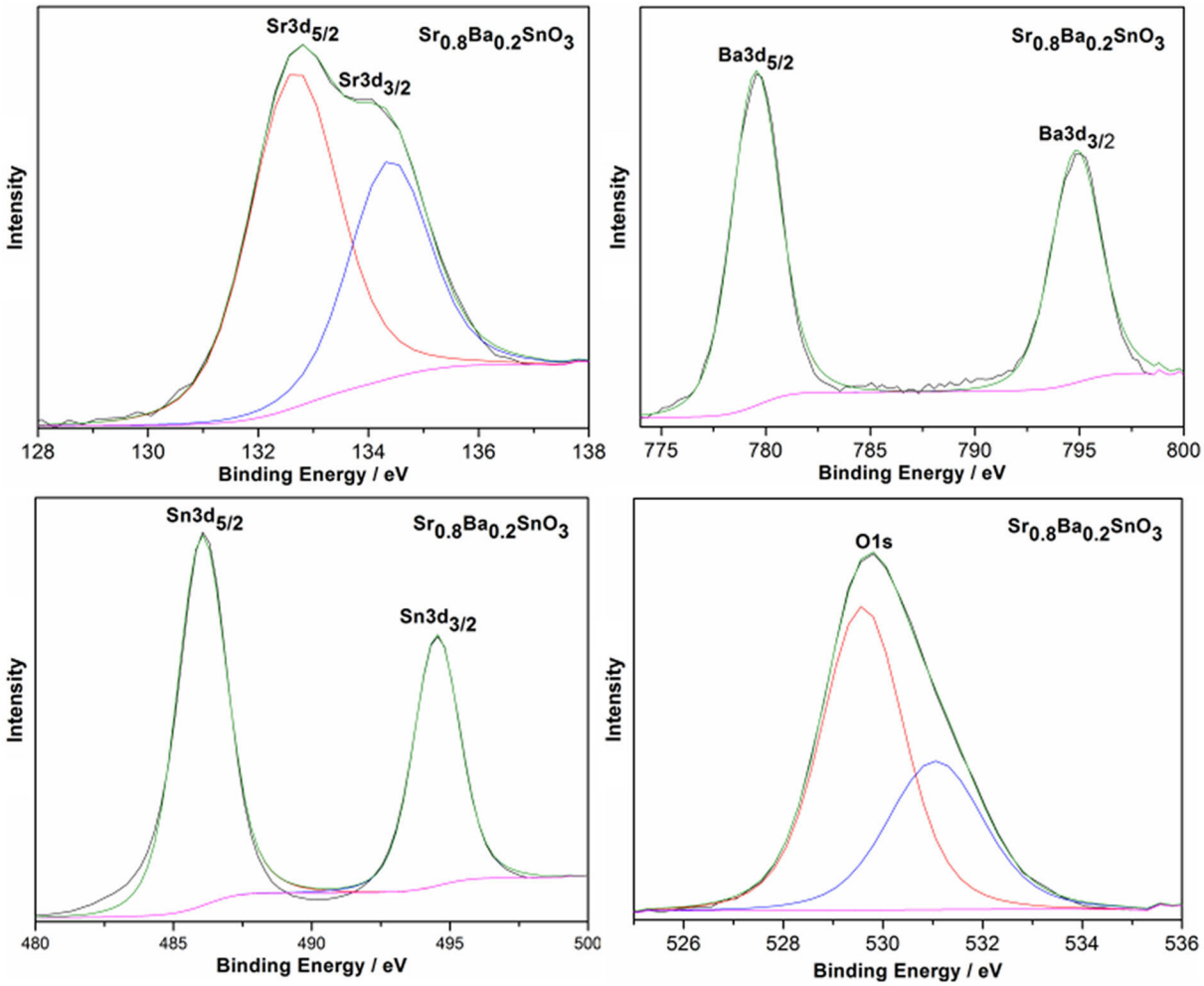

Figure 8. Detailed XPS scans of the Sr 3d, Ba 3d, Sn 3d, and O 1s regions for $Sr_{0.8}Ba_{0.2}SnO_3$.

Table 4. Band gap, electronegativity, and band-edge position for $Sr_{1-x}Ba_xSnO_3$.

Sample	Band gap [eV]	Electronegativity [eV]	E_c (NHE) [eV]	E_v [eV]
$SrSnO_3$	3.85 ± 0.02	5.537	−0.89 ± 0.04	2.96 ± 0.04
$Sr_{0.8}Ba_{0.2}SnO_3$	3.54 ± 0.02	5.522	−0.75 ± 0.04	2.79 ± 0.04
$Sr_{0.6}Ba_{0.4}SnO_3$	3.34 ± 0.02	5.506	−0.66 ± 0.04	2.68 ± 0.04
$Sr_{0.2}Ba_{0.8}SnO_3$	3.15 ± 0.02	5.475	−0.60 ± 0.04	2.55 ± 0.04
$BaSnO_3$	3.10 ± 0.02	5.460	−0.59 ± 0.04	2.51 ± 0.04

decrease in the band gap of $Sr_{1-x}Ba_xSnO_3$ with increasing Ba content can be attributed to the decrease of the Sn-centered octahedral tilting. Moreover, the increase in symmetry from orthorhombic to cubic (and the associated change of the Sn–O–Sn angle to 180°) leads to an increase in the Sn 5s nonbonding character of the conduction-band minimum. Therefore, the Sn–O 2p contribution becomes less important. As the Sn–O–Sn bonds become increasingly linear, the conduction band will be expanded, and the band-gap curves will correspondingly decrease.[5]

Furthermore, the band gaps found for $SrSnO_3$ and $BaSnO_3$ (Table 2) are lower than those reported for $SrSnO_3$ prepared through a solid-state reaction (4.1 eV)[34] or by a microwave-assisted hydrothermal method (4.27 eV)[19] and for $BaSnO_3$ synthesized by a microwave-assisted hydrothermal method (4.5 eV).[8] However, the band gap of the $BaSnO_3$ sample is equal to the value reported for $BaSnO_3$ prepared by a solid-state reaction (3.1 eV).[35]

The band-edge position can be calculated according to the method of Butler and Ginley [Eq. (2)]:[36]

$$E_c = X - E_0 - 0.5\,E_g \quad (2)$$

where E_c is the conduction-band (CB) edge potential, X is the geometric mean of the Sanderson electronegativity of the constituent atoms, E_g is the band-gap energy, and E_0 is a scale factor relating the redox level of the reference electrode to the absolute vacuum level [E_0 = 4.5 eV for a normal hydrogen electrode (NHE)]. The values for the bottom CB level of the $Sr_{1-x}Ba_xSnO_3$ samples are shown in Table 4. They range from −0.89 eV for $SrSnO_3$ to −0.59 eV for $BaSnO_3$. Thus, the valence-

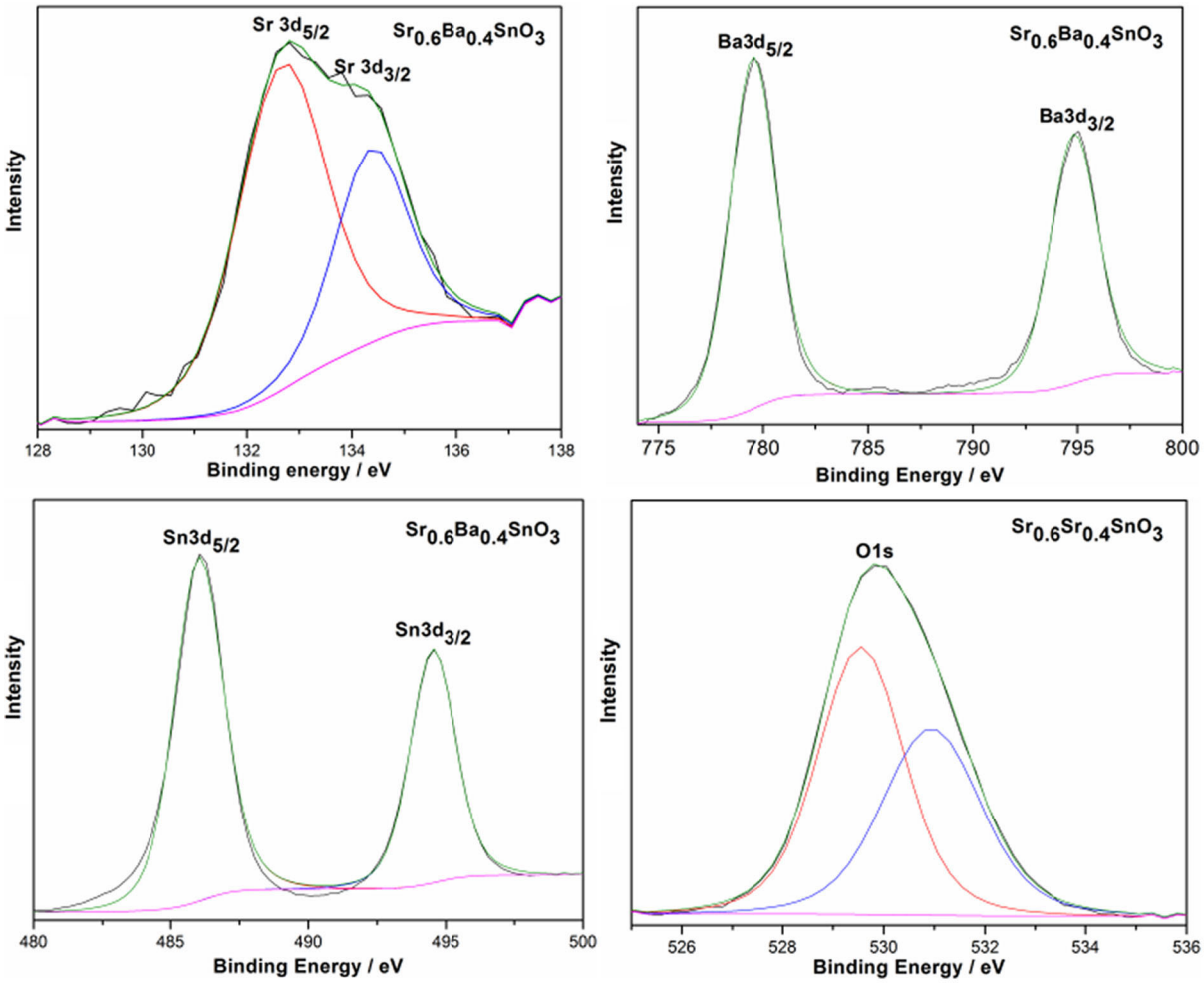

Figure 9. Detailed XPS scans of the Sr 3d, Ba 3d, Sn 3d, and O 1s regions for $Sr_{0.6}Ba_{0.4}SnO_3$.

band (VB) edge potentials vary from 2.96 eV for $SrSnO_3$ to 2.51 eV for $BaSnO_3$. The CB edges of all of the samples are more negative versus the NHE than $E^{\circ}(O_2/^{\bullet}O^{-}_2)$ (−0.33 V vs. NHE), and the VB edges (E_{VB}) of all of the samples are more positive than $E^{\circ}(^{\bullet}OH/H_2O)$ (2.3 V vs. NHE). These results show that the band-edge positions of all of the $Sr_{1-x}Ba_xSnO_3$ samples meet the electrochemical requirements for the hydroxylation of terephthalic acid (TA) under UV irradiation. Therefore, the photogenerated electrons and holes should generate the active species in photocatalytic reactions through reactions with adsorbed oxygen, hydroxide radicals, and water molecules on the surface of the photocatalyst.

The photoluminescence (PL) emission results from the recombination of photogenerated electron and hole pairs.[37] Therefore, the PL spectra of the photocatalyst can provide information about the separation efficiency of the charge carriers. The PL emission spectra of the $Sr_{1-x}Ba_xSnO_3$ samples recoded with excitation at $\lambda = 300$ nm are shown in Figure 13. All of the samples display a broad emission band centered at $\lambda \approx 383$ nm, which is ascribed to the occurrence of medium-range order–disorder in the crystalline structure generated by defects such as oxygen vacancies.[18] Moreover, it can be inferred that a high PL emission intensity relates to a low separation rate and low photocatalytic activity. From Figure 13, it can be observed that the intensity of the PL emission peak of the $Sr_{0.8}Ba_{0.2}SnO_3$ sample is the weakest, and this suggests that it has the lowest recombination rate for photogenerated charge carriers and the maximum lifetime, which should lead to improved photocatalytic activity of the catalyst.

The textural properties of the $Sr_{1-x}Ba_xSnO_3$ samples were identified by measuring their surface areas, pore volumes, and pore sizes (Table 5). The hysteresis loops for the nitrogen ad-

Table 5. Photoluminescence signal intensity of 2-hydroxyterephthalic acid (TAOH) at $\lambda = 426$ nm and sample surface area.

Sample	TAOH intensity[a]	BET surface area [$m^2 g^{-1}$]	Pore diameter [nm]	Pore volume [$cm^3 g^{-1}$]
$SrSnO_3$	728	3.55	11.70	0.010
$Sr_{0.8}Ba_{0.2}SnO_3$	973	15.82	18.24	0.072
$Sr_{0.6}Ba_{0.4}SnO_3$	328	6.75	14.31	0.024
$Sr_{0.2}Ba_{0.8}SnO_3$	187	7.01	15.10	0.026
$BaSnO_3$	497	4.80	17.41	0.020

[a] After 120 min irradiation.

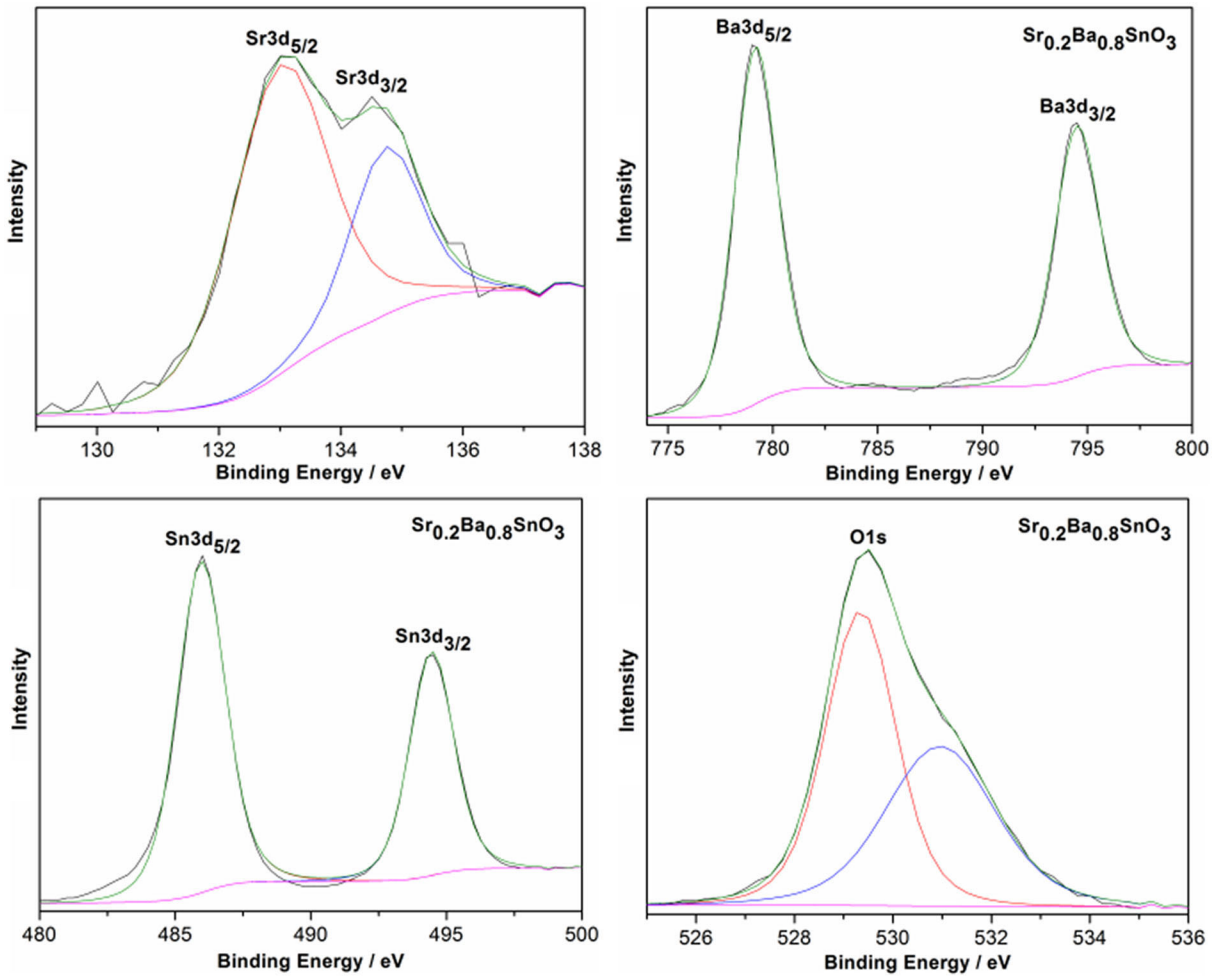

Figure 10. Detailed XPS scans of the Sr 3d, Ba 3d, Sn 3d, and O 1s regions for $Sr_{0.2}Ba_{0.8}SnO_3$.

sorption–desorption experiments on the $Sr_{1-x}Ba_xSnO_3$ samples are given in Figure 14. The isotherms of the obtained samples are of type IV, which indicates mesoporosity. The pore-size distributions of the $Sr_{1-x}Ba_xSnO_3$ samples were estimated from the adsorption branch by the Barrett–Joyner–Halenda (BJH) method. The pore sizes vary from 11.7 nm for $SrSnO_3$ to 18.24 nm for $Sr_{0.8}Ba_{0.2}SnO_3$. The mesoporosity of the samples can be ascribed to the spaces between the $Sr_{1-x}Ba_xSnO_3$ particles. The specific surface areas range from 3.55 m^2g^{-1} for $SrSnO_3$ to 15.82 m^2g^{-1} for $Sr_{0.8}Ba_{0.2}SnO_3$.

Photocatalytic activity of $Sr_{1-x}Ba_xSnO_3$ for photohydroxylation of terephthalic acid

The photohydroxylation activities of the prepared $Sr_{1-x}Ba_xSnO_3$ samples were evaluated by testing the materials as photocatalysts in the selective oxidation of terephthalic acid (TA) under UV irradiation (Table 5). A proposed mechanism for this photocatalytic reaction is shown Figure 15. If the photocatalyst is irradiated by light with energy equal to or larger than its band gap, electrons are promoted from the valence band to the conduction band, and holes are generated in the valence band. The electrons and holes either migrate to the surfaces of the particles or undergo an undesired recombination. The holes react with adsorbed water molecules to generate $^{\bullet}OH$ radicals, which can react with TA to form 2-hydroxyterephthalic acid (TAOH). The latter shows a characteristic fluorescence band at $\lambda = 426$ nm.[38,39] As an example, the changes to the fluorescence spectra of TA under UV irradiation in the presence of $Sr_{0.8}Ba_{0.2}SnO_3$ are shown in Figure 16. The maximum intensity change of TAOH as a function of irradiation time during the TA hydroxylation over the different $Sr_{1-x}Ba_xSnO_3$ samples is shown in Figure 17. The linear development of the maximum fluorescence of TAOH at $\lambda = 426$ nm with irradiation time seems to indicate the stability of the catalyst samples. There is no hydroxylation of TA in the absence of the photocatalysts. However, the photocatalytic activities of the $Sr_{1-x}Ba_xSnO_3$ samples are diverse and follow the order $Sr_{0.8}Ba_{0.2}SnO_3 > SrSnO_3 > BaSnO_3 > Sr_{0.6}Ba_{0.4}SnO_3 > Sr_{0.2}Ba_{0.8}SnO_3$. As shown in Figure 17, the $Sr_{0.8}Ba_{0.2}SnO_3$ sample, with an average crystallite size of 35.4 nm and specific surface area of 15.8 cm^3g^{-1}, exhibited superior photocatalytic activity to the $Sr_{0.2}Ba_{0.8}SnO_3$ sample with an average crystallite size of 47.3 nm and specific surface area of 6.9 cm^3g^{-1}. As illustrated in Table 5 and Figure 17, the $Sr_{0.8}Ba_{0.2}SnO_3$ sample reveals a photooxidation potential that is 1.3, 1.96, 3, and 5.2 times higher than those of $SrSnO_3$, $BaSnO_3$,

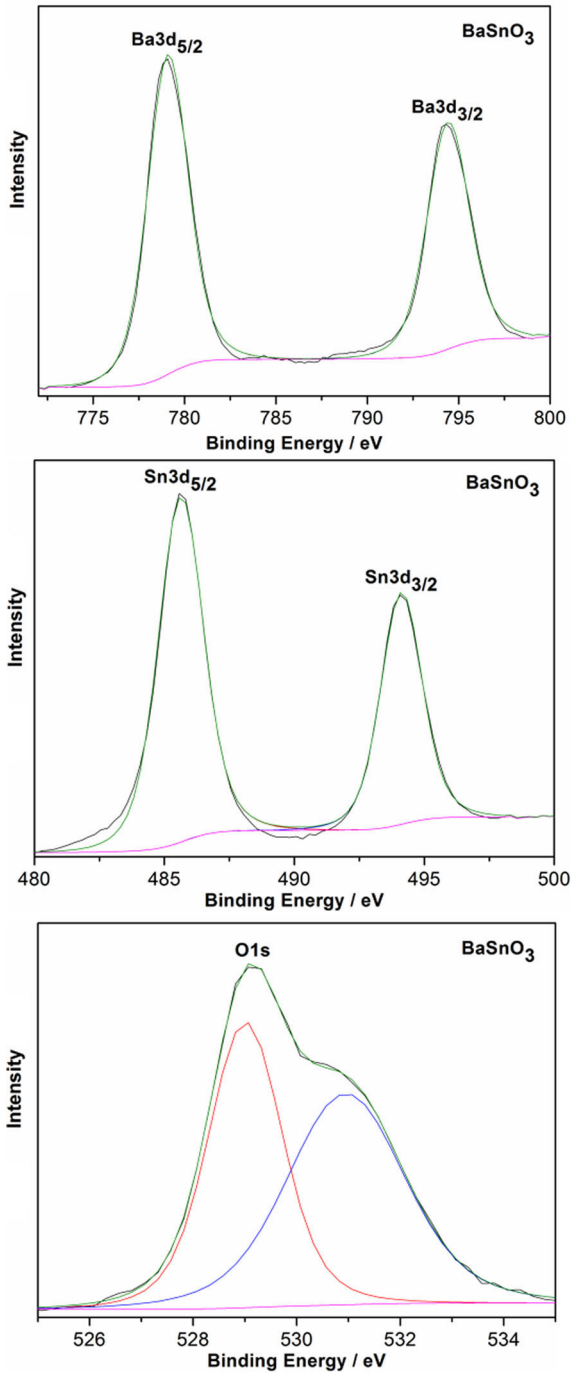

Figure 11. Detailed XPS scans of the Ba 3d, Sn 3d, and O 1s regions $BaSnO_3$.

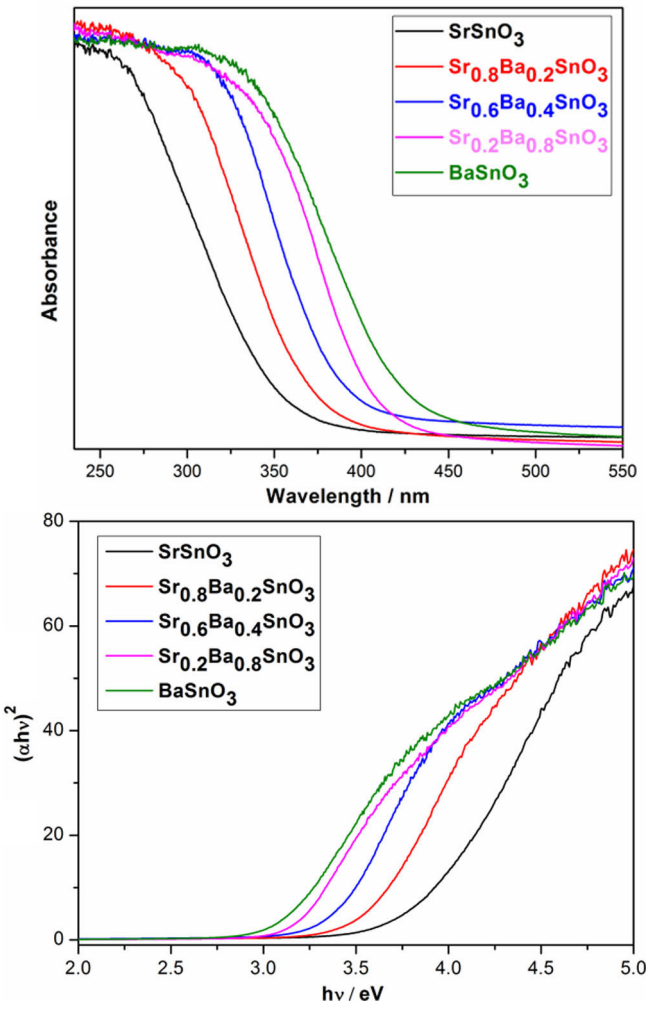

Figure 12. Top: UV/Vis absorption spectra of the $Sr_{1-x}Ba_xSnO_3$ samples. Bottom: $(\alpha h\nu)^2$ versus $h\nu$ curves

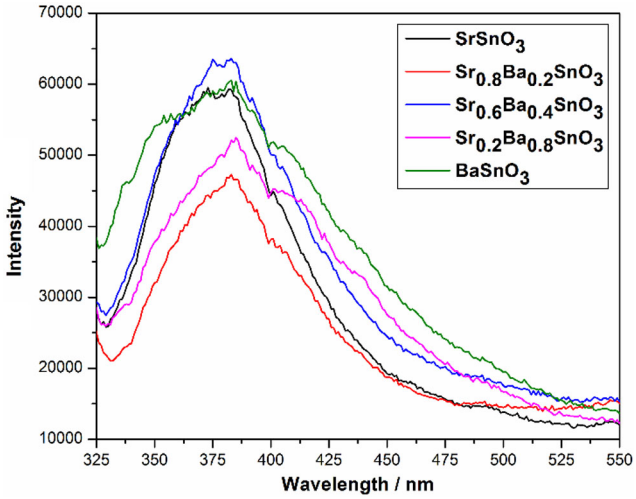

Figure 13. Photoluminescence spectra of the $Sr_{1-x}Ba_xSnO_3$ samples (excitation wavelength: 300 nm).

$Sr_{0.6}Ba_{0.4}SnO_3$, and $Sr_{0.2}Ba_{0.8}SnO_3$, respectively. The results from the PL measurements suggest that the superior photocatalytic activity of $Sr_{0.8}Ba_{0.2}SnO_3$ can be ascribed to the enhanced separation of the photogenerated charge carriers. However, this enhanced capacity to generate $^{\bullet}OH$ radicals for the $Sr_{0.8}Ba_{0.2}SnO_3$ sample can be attributed to several reasons including the increased surface-area/volume ratio, the smaller crystallite size, and the more negative CB minimum (−0.75 V) than that of $O_2/O_2^{\bullet-}$ (−0.33 V). Photocatalysts with high surface areas provide a large number of adsorption sites and, thereby, the recombination of photoinduced charge carriers is reduced. The particle size influences the separation of the charge carri-

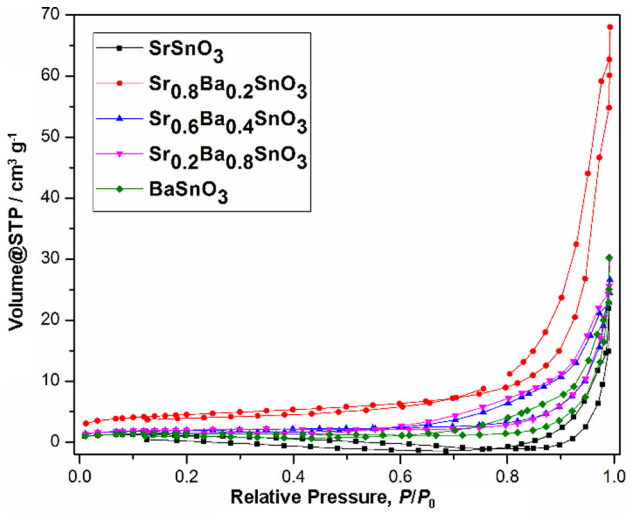

Figure 14. N_2 adsorption–desorption isotherms of the $Sr_{1-x}Ba_xSnO_3$ samples.

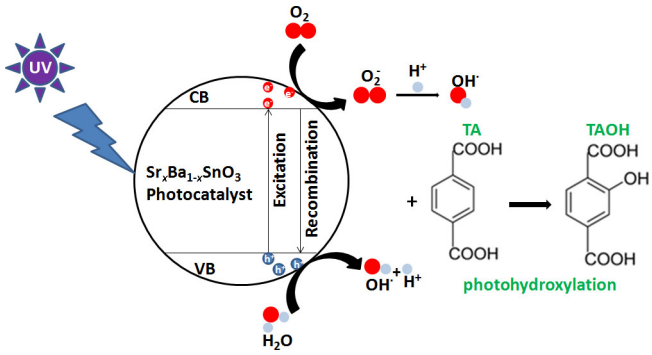

Figure 15. Mode of action of the $Sr_{1-x}Ba_xSnO_3$ photocatalysts for the hydroxylation of TA.

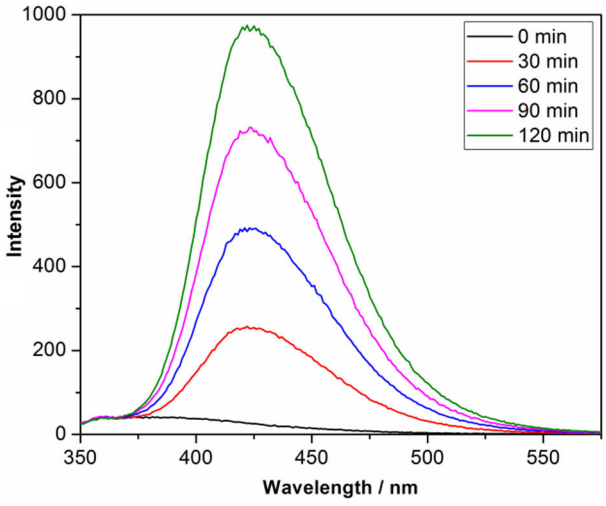

Figure 16. Emission spectra (intensity vs. wavelength) as a function of illumination time for the photohydroxylation of TA with $Sr_{0.8}Ba_{0.2}SnO_3$; excitation wavelength 320 nm.

ers through a reduction of the recombination possibility.[40] The more negative level of the bottom of the conduction band

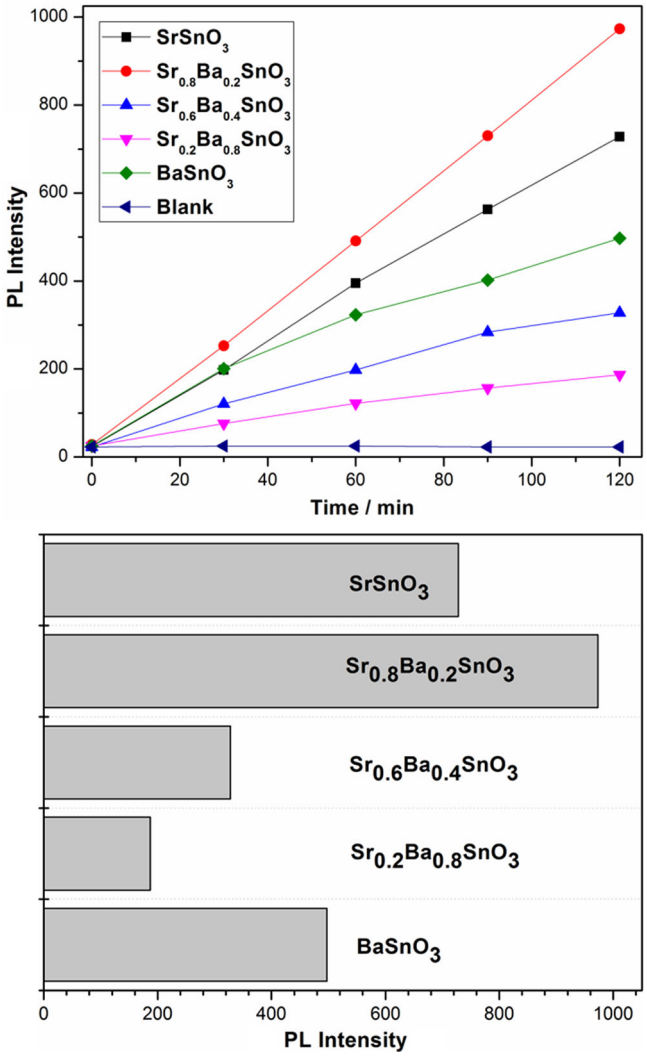

Figure 17. Top: maximum intensity of the photoluminescence emission of TAOH at $\lambda = 426$ nm as a function of irradiation time during the hydroxylation of TA over $Sr_{1-x}Ba_xSnO_3$ samples. Bottom: maximum intensities after 120 min of irradiation over $Sr_{1-x}Ba_xSnO_3$ samples (bottom).

leads to better redox ability for the photoinduced electrons. On the other hand, the XRD data showed that $Sr_{0.8}Ba_{0.2}SnO_3$ has distorted SnO_6 octahedra with bent Sn–O–Sn angles. This distortion enhances the photocatalytic activity because it improves charge separation, as local fields in the interior of the distorted polyhedra provoke and also ease the separation of the charge carriers.[9] Furthermore, the crystal-strain evaluation shows that the crystallinity of $Sr_{0.2}Ba_{0.8}SnO_3$ is higher than that of the $Sr_{0.8}Ba_{0.2}SnO_3$ sample. Therefore, the main reason for the different photocatalytic activities of the samples is not the variation in their crystallinity.

To our knowledge, there are no reports relating to the use of stannates in the photohydroxylation of terephthalic acid. Recently, some efforts were devoted to the use of stannates as photocatalysts for water splitting and wastewater treatment. Sales et al.[41] investigated the photodegradation of an azo dye over $Sr_{1-x}Ba_xSnO_3$ ($x = 0$, 0.25, 0.5, 0,75, 1). They observed a linear decrease of the photodegradation ability with decreas-

ing barium concentration. The activities followed the order $BaSnO_3 > Sr_{0.25}Ba_{0.75}SnO_3 > Sr_{0.5}Ba_{0.5}SnO_3 > Sr_{0.75}Ba_{0.25}SnO_3 > SrSnO_3$. Their findings indicated that the highest activity of $BaSnO_3$ can be attributed to the preferable direct oxidation mechanism as a consequence of the high ionic character of the Ba^{2+}–O^{2-} bonds, which lead to active-site interactions with the azo dye, higher adsorption character, and, thereby, a higher degree of photodegradation. The results reported herein differ completely from those presented by Sales et al. because the indirect mechanism (photogenerated electrons react with the adsorbed O_2 on the surface of catalyst) is more efficient for the photohydroxylation of TA than the direct mechanism (photogenerated electrons react directly with the adsorbed organic molecules on the surface of the catalyst). Yuan et al.[5] reported the use of $Sr_{1-x}Ba_xSnO_3$ ($x = 0$, 0.25, 0.5, 0,75, 1) as photocatalysts for water splitting. The H_2 generation rates decreased with increasing Ba content in the order $SrSnO_3 > Sr_{0.75}Ba_{0.25}SnO_3 > Sr_{0.5}Ba_{0.5}SnO_3 > Sr_{0.25}Ba_{0.75}SnO_3 > BaSnO_3$. Yuan et al. attributed the better performance of $SrSnO_3$ to the enhanced reduction ability of the photogenerated electrons in addition to the enhanced charge-carrier transport. The two factors are related to the electronegativity of the Sr^{2+} cations and the short Sn–O bond length resulting from the increasing octahedral tilting distortion with decreasing Ba concentration. Wang et al.[19] evaluated the photocatalytic activities of $MSnO_3$ (M = Ca, Sr, Ba) for the degradation of methyl orange. In their study, the activities followed the order $CaSnO_3 > SrSnO_3 > BaSnO_3$. The photocatalytic activities are strongly dependent on the distortion of the SnO_6 units in the crystal structures of the stannates, and the increase of the M^{2+} ionic radius leads to a decrease in the distortion of the SnO_6 octahedra and lower photocatalytic activity. Although the order of the photocatalytic activities of $SrSnO_3$ and $BaSnO_3$ in this study agree with previous reports by Wang et al., we cannot attribute the different activities for $S_{1-x}Ba_xSnO_3$ only to the differences in the crystal structures. We believe that the catalytic activity depends on the synergistic impacts of different factors such as the surface area associated with the crystal structure and an appropriate energy band structure.

Furthermore, the photocatalyst stability was evaluated by performing three photohydroxylation experiments of TA over recycled $Sr_{0.8}Ba_{0.2}SnO_3$ under the same reaction conditions (Figure 18). For each cycle, the photocatalyst was collected by centrifugation, washed twice with deionized water, and dried overnight at 80 °C. Moreover, for every cycle, a fresh TA solution was used under the consideration of the loss of photocatalyst during the sampling procedure. The XRD patterns of the $Sr_{0.8}Ba_{0.2}SnO_3$ sample before and after photohydroxylation (Figure 19) confirm that no noteworthy changes to the structure occurred during the three successive runs. From Figure 18, it can be concluded that the $Sr_{0.8}Ba_{0.2}SnO_3$ sample has good stability over three cycles.

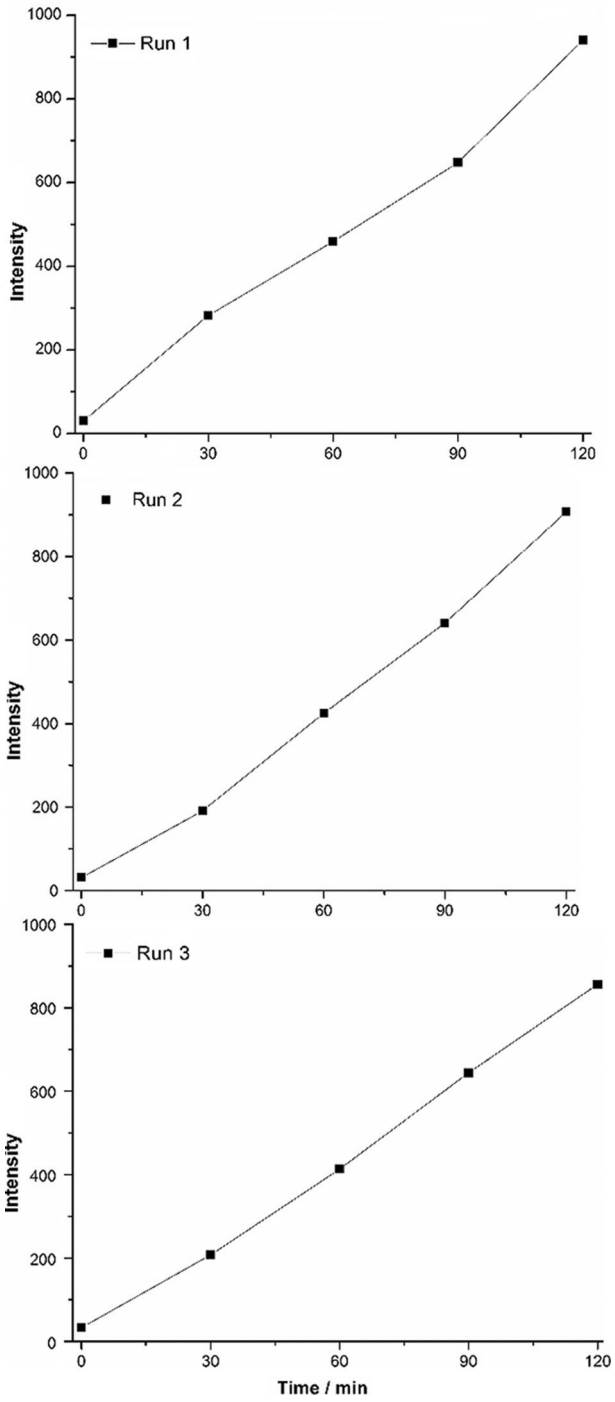

Figure 18. Reusability of the $Sr_{0.8}Ba_{0.2}SnO_3$ sample after three successive runs.

Effect of the preparation method

To study the influence of preparation method on the structure, morphology, and photocatalytic activity, $SrSnO_3$ was prepared ionothermally through conventional heating. The other reaction conditions were kept unchanged. The XRD pattern of the ionothermally prepared $SrSnO_3$ sample is shown in Figure SI-7. In addition to the diffraction peaks of orthorhombic SrSnO, small peaks can be observed at $2\theta = 25.14$, 25.8, and 44°. These peaks correspond to $SrCO_3$ (ICSD 15195). Furthermore, the peak at $2\theta = 26.6°$ can be indexed to SnO_2 (ICSD 9163). From the Scherrer equation, the crystal-domain size of the ionothermally prepared sample was estimated to be (51 ± 1) nm.

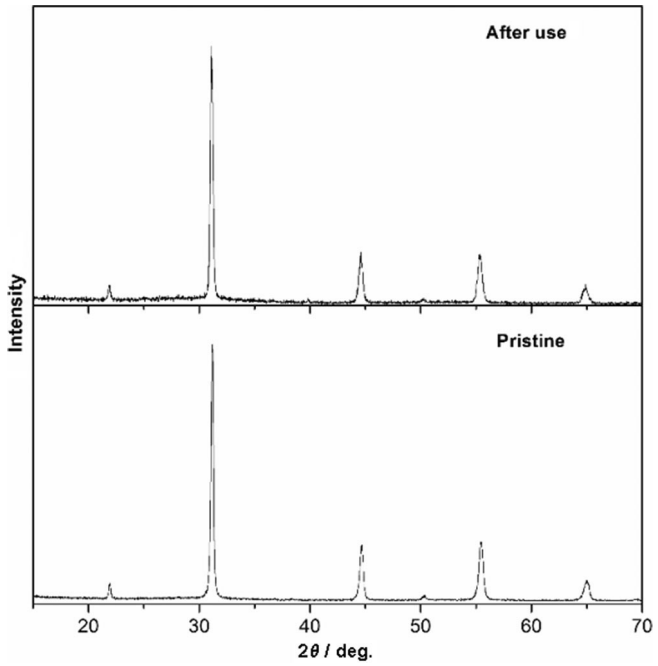

Figure 19. XRD patterns before and after photohydroxylation.

As shown in Figure 20, the SEM image of ionothermally prepared $SrSnO_3$ displays the formation of sheetlike particles, which are agglomerated to form chrysanthemum-like microstructures. The BET surface area of the ionothermally prepared $SrSnO_3$ (2.75 $m^2 g^{-1}$) is lower than that of $SrSnO_3$ prepared by microwave synthesis (3.55 $m^2 g^{-1}$). The catalytic activity of the ionothermally prepared $SrSnO_3$ is compared with those of the samples prepared by microwave irradiation in Figure 21. The ionothermally prepared sample shows a higher activity than those of the samples prepared by microwave synthesis because of the impact of the SnO_2 and $SrCO_3$ side-phases. The formed composites can suppress the recombination of charge carriers at the surface of the ionothermally prepared sample. This assumption can be confirmed by the PL spectra of the samples. The lower intensity of the PL emission peak for ionothermally prepared $SrSnO_3$ than that of $SrSnO_3$ prepared by microwave (Figure SI-8) indicates that the recombination of charge carriers in the ionothermally prepared sample is efficiently suppressed compared with that of its counterpart, and this leads to an enhanced photohydroxylation activity.

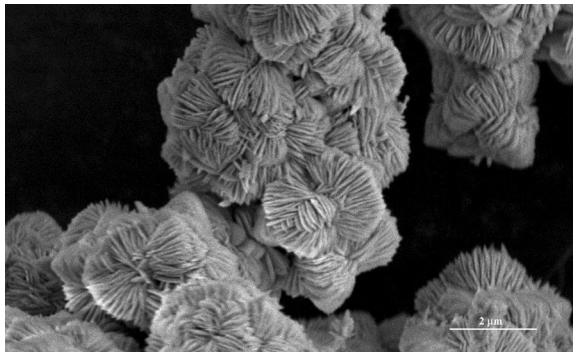

Figure 20. SEM image of $SrSnO_3$ obtained ionothermally. Scale bar corresponds to 2 μm.

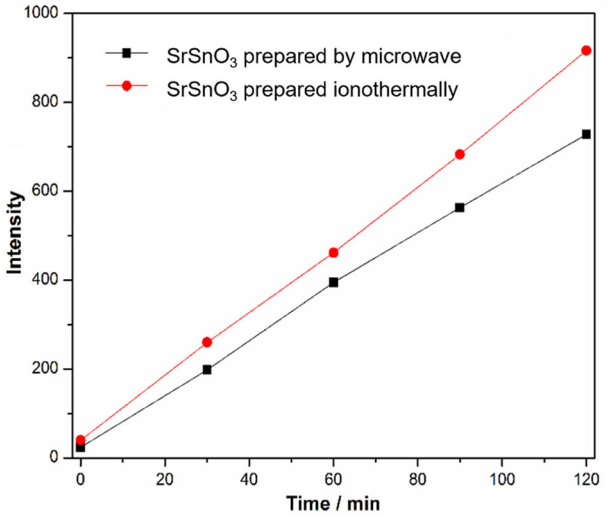

Figure 21. TA hydroxylation over $SrSnO_3$ samples obtained by microwave and ionothermal methods.

Conclusions

We have synthesized photocatalytically active perovskite nanocrystals of compositions $SrSnO_3$ and $BaSnO_3$ as well as their $Sr_{1-x}Ba_xSnO_3$ solid solutions by microwave irradiation in an ionic liquid (IL) and subsequent heat-treatment. This method is rapid, facile and reproducible, and no template or surfactant is required (as the IL acts as solvent and a template). The IL also serves as a heating medium under microwave reaction and can be recycled readily for photocatalysis. The substitution of Ba into $SrSnO_3$ affects the morphology, crystallinity, and photocatalytic activity. The increasing Ba concentration leads to structural changes in the perovskite structure from *Pnma* for $x=0$ and 0.2 to *Imma* for $x=0.4$ and $Pm\bar{3}m$ for $x=0.8$, 1. The $BaSnO_3$ sample shows the highest crystallinity, whereas the $Sr_{0.8}Ba_{0.2}SnO_3$ sample is the least crystalline material. All of the $Sr_{1-x}Ba_xSnO_3$ samples prepared through microwave reactions in IL favor the formation of rodlike shapes. With increasing Ba content in the lattice of $SrSnO_3$, the diameter of the rods increases, and their homogeneity decreases. The $Sr_{1-x}Ba_xSnO_3$ samples showed different catalytic activities for the photohydroxylation of terephthalic acid (TA) under UV irradiation. The highest photocatalytic activity was observed for $Sr_{0.8}Ba_{0.2}SnO_3$, and the order of the activities for TA hydroxylation was $Sr_{0.8}Ba_{0.2}SnO_3 > SrSnO_3 > BaSnO_3 > Sr_{0.6}Ba_{0.4}SnO_3 > Sr_{0.2}Ba_{0.8}SnO_3$. The photocatalyst remains stable and can be reused multiple times. This can be explained by the enhanced charge-carrier separation along with improved reduction ability of the photoinduced electrons. This appears to be a result of the synergistic effects of the relatively large surface area associated with lattice distortion, the small crystallite size, and sufficient energy band structure.

Experimental Section

Materials

Chemicals were purchased from Iolitec [lithium bis(trifluoromethanesulfonyl)amide, 99%], Sigma–Aldrich [tin(VI) chloride pentahydrate, 98%; 1-methylimidazole, 99%; ethanol (p.a.), 1-chlorobutane, 99%], Fisher Scientific (sodium hydroxide, 98%), J. T. Baker (acetonitrile, 99.5%; ethylacetate, 99%), Alfa Aesar (strontium acetate hydrate, 98%; barium acetate, 99%; terephthalic acid, 98%). All reagents employed were commercially available and used directly without further purification. The ionic liquid [C_4mim][Tf_2N] was prepared by a modified literature procedure.[42]

Synthesis of $Sr_{1-x}Ba_xSnO_3$ ($x = 0$, 0.2, 0.4, 0.8, 1)

For the synthesis of the $Sr_{1-x}Ba_xSnO_3$ samples, stoichiometric amounts of $Ba(CH_3COO)_2$, $Sr(CH_3COO)_2{\cdot}0.5\,H_2O$, and $SnCl_4$ to give approximately 100 mg of the final product and finely ground NaOH powder (0.15 g) were added to a mixture of deionized water (1 mL) and [C_4mim][Tf_2N] (2 mL). The reaction mixture was stirred vigorously for 30 min and then irradiated with a single-mode microwave synthesizer (CEM Discover) operating at a frequency of 2455 MHz in a 10 mL glass vessel equipped with a Teflon septum for 10 min at 85 °C. The product was separated by centrifugation, washed thoroughly with ethanol and distilled water, and dried overnight in air at 80 °C. The dried product was calcined at 700 °C in air for 3 h.

The preparation of $SrSnO_3$ through ionothermal synthesis was performed in a 50 mL Teflon cup enclosed in a stainless-steel autoclave (Parr Instruments). The reaction mixture was transferred to the Teflon cup and sealed in the autoclave, which was put in a furnace and heated at 170 °C for 20 h. Then, the autoclave was cooled in air. The resulting powder was separated by centrifugation, washed with ethanol and deionized water several times, and dried at 80 °C overnight. The dried product was calcined at 700 °C in air for 3 h.

Characterization

The powder X-ray diffraction measurements were performed with a PANalytical powder diffractometer with an Xcelerator Detector and CuK_α radiation ($\lambda = 0.15406$ nm). The structural parameters were determined by Rietveld refinement with the FULLPROF program suite and a pseudo-Voigt peak-shape function.[43]

The XPS measurements were performed with a Physical Electronics 5500 Multitechnique system with a standard aluminium source. The analysis spot size was 1×1 mm. The samples were mounted on double-sided Scotch tape. The BEs in the XPS spectra were calibrated against the C 1s signal (BE = 284.8 eV) of adventitious physisorbed carbon.

The SEM measurements were performed with a high-resolution thermally aided field SEM instrument (Zeiss, LEO 1530 Gemini) with a field-emission gun (FEG) and an acceleration voltage of U_{acc} = 0.2–30 kV. For the SEM measurements the $Sr_{1-x}Ba_xSnO_3$ powders were placed on a carbon-film, which was dried under vacuum for 20 min.

The nitrogen physisorption experiments were performed at 78 K with a Micromeritics Tristar analyzer. The samples were pretreated thermally at 100 °C for 6 h under flowing N_2. The surface areas were calculated by the BET method.

The UV/Vis spectra were measured at room temperature in reflection mode with an Agilent Cary 60 spectrometer with a dip probe coupler (Agilent) and a VideoBarrelino probe (Harrick).

The PL spectra were recorded with an Agilent Technologies Cary Eclipse fluorescence spectrophotometer equipped with a xenon flash lamp and built-in excitation and emission filters. For the measurements, liquid samples were added to a standard 10 mm quartz cuvette, which was positioned in the incoming beam in the sample chamber.

The attenuated total reflection (ATR) IR spectroscopy was performed with an Agilent Technologies Cary 630 FTIR spectrometer equipped with a diamond crystal ATR unit. Solid samples were pressed onto the crystal.

The Raman spectra were obtained with a Horiba Xplora Raman microscope (Horiba Scientific) at 150 mW and room temperature. Laser irradiation at $\lambda = 785$ nm was used for the excitation. Silicon was used as the standard for the calibration of the Raman shifts.

Photocatalytic activity tests

The catalytic tests were performed with a reactor containing a suspension of the photocatalyst (100 mg) in 0.01 M NaOH solution (100 mL) containing 3 mM terephthalic acid. The suspension was stirred continuously in the dark for 30 min to establish the adsorption–desorption equilibrium and then illuminated with a 100 W Xe arc lamp (Newport Oriel Instruments). The lamp was switched on 30 min before the illumination of the samples to stabilize the power of its emission at $\lambda > 320$ nm (a FSQ-WG320 cutoff filter was used to eliminate most of the radiation below $\lambda = 320$ nm). Every 30 min, an aliquot (≈3 mL) was removed and filtered through a nylon syringe filter (pore size 0.2 μm) to remove the photocatalyst before analysis by fluorescence spectrometry; the fluorescence was monitored at $\lambda = 426$ nm, which corresponds to the fluorescence band of 2-hydroxyterephthalic acid (TAOH). The photogenerated holes react with surface-adsorbed water molecules to form $^{\bullet}OH$ radicals, which react with terephthalic acid to form 2-hydroxyterephthalic acid, and the TAOH exhibits a typical fluorescence band at $\lambda = 426$ nm under excitation at $\lambda = 320$ nm. Thus, an increase in the intensity of this band with time is linked directly to an increased amount of photogenerated $^{\bullet}OH$ radicals.

Conflict of interest

The authors declare no conflict of interest.

Keywords: barium · ionic liquids · microwave chemistry · perovskite phases · strontium

[1] W. F. Zhang, J. Tang, J. Ye, *Chem. Phys. Lett.* **2006**, *418*, 174–178.
[2] C. P. Udawatte, M. Kakihana, M. Yoshimura, *Solid State Ionics* **2000**, *128*, 217–226.
[3] B. Kennedy, I. Qasim, K. Knight, *J. Phys. Condens. Matter* **2015**, *27*, 365401.
[4] G. Saito, Y. Nakasugi, N. Sakaguchi, C. Zhu, T. Akiyama, *J. Alloys Compd.* **2015**, *652*, 496–502.
[5] Y. Yuan, J. Lv, X. Jiang, Z. Li, T. Yu, Z. Zou, J. Ye, *Appl. Phys. Lett.* **2007**, *91*, 094107.
[6] A. Stanulis, S. Sakirzanovas, M. Van Bael, A. Kareiva, *J. Sol-Gel Sci. Technol.* **2012**, *64*, 643–652.
[7] J. Ahmed, C. Blakely, S. Bruno, V. Poltavets, *Mater. Res. Bull.* **2012**, *47*, 2282–2287.

[8] S. Moshtaghi, S. Gholarmrezaei, M. S. Niasari, P. Mehdizadeh, *J. Mater. Sci. Mater. Electron.* **2016**, *27*, 414 – 424.
[9] S. Wang, M. Lu, G. Zhou, Y. Zhou, A. Zhang, Z. Yang, *J. Alloys Compd.* **2007**, *432*, 265 – 268.
[10] D. Chen, J. Ye, *Chem. Mater.* **2007**, *19*, 4585 – 4591.
[11] A. Jadhav, A. Lim, G. Thorat, H. Jadhav, J. Seo, *RSC Adv.* **2016**, *6*, 31675 – 31686.
[12] S. Motshekga, S. Pillai, S. Ray, K. Jalama, R. Krause, *J. Nanomater.* **2012**, 691503.
[13] *Handbook of Green Chemistry Vol. 6: Green Solvents, Ionic Liquids* (Eds.: P. T. Anastas, P. Wasserscheid, A. Stark), Wiley-VCH, Weinheim, **2013**.
[14] A. V. Mudring, T. Alammar, T. Bäcker, K. Richter in *Ionic Liquids: From Knowledge to Application* (Eds.: N. V. Plechkova, R. D. Rogers, K. R. Seddon), American Chemical Society, Washington, DC, **2009**, pp. 177 – 188.
[15] H. Lu, P. Zhang, Z.-A. Qiao, J. Zhang, H. Zhu, J. Chen, Y. Chena, S. Dai, *Chem. Commun.* **2015**, *51*, 5910 – 5913.
[16] Y.-Y. Dong, J. He, S.-L. Sun, M.-G. Ma, I.-H. Fu, R.-C. Sun, *Carbohydr. Polym.* **2013**, *98*, 168 – 173.
[17] T. Alammar, Y.-K. Chow, A.-V. Mudring, *New J. Chem.* **2015**, *39*, 1339 – 1347.
[18] J. Bohnemann, R. Libanori, M. Moreira, E. Longo, *Chem. Eng. J.* **2009**, *155*, 905 – 909.
[19] W. Wang, S. Liang, K. Ding, J. Bi, J. Yu, P. Wong, L. Wu, *J. Mater. Sci.* **2014**, *49*, 1893 – 1902.
[20] F. A. Rabuffetti, J. S. Lee, R. L. Brutchey, *Chem. Mater.* **2012**, *24*, 3114 – 3116.
[21] G. K. Williamson, W. H. Hall, *Acta Metall.* **1953**, *1*, 22 – 31.
[22] C. Li, Y. Zhu, S. M. Fang, H. Wang, Y. Gui, L. Bi, R. Chen, *J. Phys. Chem. Solids* **2011**, *72*, 869 – 874.
[23] H, Weingärtner, *Angew. Chem. Int. Ed.* **2008**, *47*, 654 – 670; *Angew. Chem.* **2008**, *120*, 664 – 682.
[24] *Ionic Liquids, Theory, Properties, New Approaches* (Ed.: A. Kokorin), InTech, Rijeka, **2011**.
[25] L. Wang, L. Chang, B. Zhang, Z. Yuan, G. Shao, W. Zheng, *Inorg. Chem.* **2008**, *47*, 1443 – 1452.
[26] T. Gutel, C. C. Santini, K. Philippot, A. Padua, K. Pelzer, B. Chaudret, Y. Chauvin, J. M. Basset, *J. Mater. Chem.* **2009**, *19*, 3624 – 3631.
[27] M. Licheron, G. Jouan, E. Husson, *J. Eur. Ceram. Soc.* **1997**, *17*, 1453 – 1457.
[28] E. Moreira, J. M. Henriques, D. L. Azevedo, E. W. S. Caetano, V. N. Freire, E. L. Albuquerque, *J. Solid State Chem.* **2011**, *184*, 921 – 928.
[29] T. M. Lobo, R. Lebullenger, V. Bouquet, M. Guilloux-Viry, I. Santos, I. Weber, *J. Alloys Compd.* **2015**, *649*, 491 – 494.
[30] P. Jayabal, V. Sasirekha, J. Mayandi, K. Jaganathan, V. Ramakrishnan, *J. Alloys Compd.* **2014**, *586*, 456 – 461.
[31] S. Das, D.-Y. Kim, C.-M. Choi, Y.-B. Hahn, *Mater. Res. Bull.* **2011**, *46*, 609 – 614.
[32] F. Zhong, H. Zhuang, Q. Gu, J. Long, *RSC Adv.* **2016**, *6*, 42474 – 42481.
[33] N. Sharma, K. M. Shju, G. V. S. Rao, B. V. R. Chowdari, *J. Power Sources* **2005**, *139*, 250 – 260.
[34] C. W. Lee, D. W. Kim, I. S. Cho, S. Park, S. S. Shin, S. W. Seo, K. S. Hong, *Int. J. Hydrogen Energy* **2012**, *37*, 10557 – 10563.
[35] W. Zhang, J. Tang, J. Ye, *J. Mater. Res.* **2007**, *22*, 1859 – 1871.
[36] M. A. Butler, D. S. Ginley, *J. Electrochem. Soc.* **1978**, *125*, 228 – 232.
[37] K. Nagaveni, M. S. Hegde, G. Madras, *J. Phys. Chem. B* **2004**, *108*, 20204 – 20212.
[38] H. Dong, G. Chen, J. Sun, C. Li, Y. Yu, D. A. Chen, *Appl. Catal. B* **2013**, *134*, 46 – 54.
[39] L. Schwertmann, A. Grünert, A. Pougin, C. Sun, M. Wark, R. Marschall, *Adv. Funct. Mater.* **2015**, *25*, 905 – 912.
[40] A. Kudo, Y. Miseki, *Chem. Soc. Rev.* **2009**, *38*, 253 – 278.
[41] H. B. Sales, V. Bouquet, S. Deputier, S. Ollivier, F. Gouttefangeas, I. M. G. Dos Santos, *Solid State Sci.* **2014**, *28*, 67 – 73.
[42] P. Webb, M. Sellin, T. Kunene, S. Williamson, A. Slawin, D. Cole-Hamilton, *J. Am. Chem. Soc.* **2003**, *125*, 15577 – 15588.
[43] J. Rodríguez-Carvajal, *FULLPROF Program for Rietveld Refinement,* Laboratorie Leon Brillouin, CEA-Saclay, **2000**.

Manuscript received: April 11, 2017
Revised manuscript received: May 31, 2017
Accepted manuscript online: June 6, 2017
Version of record online: ■■ ▮▮, 0000

*T. Alammar, I. I. Slowing, J. Anderegg, A.-V. Mudring**

■■ – ■■

Ionic-Liquid-Assisted Microwave Synthesis of Solid Solutions of $Sr_{1-x}Ba_xSnO_3$ Perovskite for Photocatalytic Applications

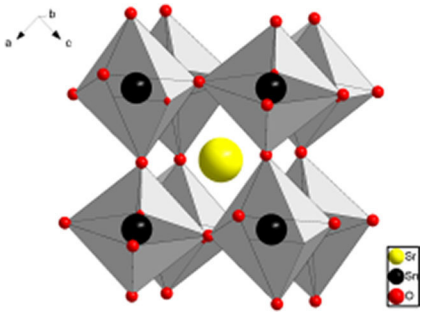

Raising the barium: A sustainable procedure for the preparation of $Sr_{1-x}Ba_xSnO_3$ perovskites for photocatalytic applications through microwave irradiation in an ionic liquid as a microwave absorbing agent, green solvent, and capping agent is presented.

